Physica Medica 62 (2019) 140–151

Contents lists available at ScienceDirect

Physica Medica

journal homepage: www.elsevier.com/locate/ejmp

Original paper

# A cell-by-cell Monte Carlo simulation for assessing radiation-induced DNA double strand breaks

Brian HeeEun Lee[a,*], C.-K. Chris Wang[b]

[a] 251 E Huron Street, Galter Pavilion L-210, Department of Radiation Oncology, Northwestern University Feinberg School of Medicine, Northwestern Memorial Hospital, Chicago, IL 60611, USA[1]

[b] 770 State St NW, Nuclear and Radiological Engineering and Medical Physics Program, Georgia Institute of Technology, Atlanta, GA 30332, USA

ARTICLE INFO

*Keywords:*
Monte Carlo method
Particle track structures
Chromatin fibers
Chromatin domains
DNA double strand breaks (DSB)
Relative biological effectiveness (RBE)

ABSTRACT

This paper presents a cell-by-cell Monte Carlo simulation study that combines charged particle track structure data with an interphase cell nucleus model to quantify DNA double strand breaks (DSBs), spatial distribution of DSBs in a cell nucleus, and resulting potentially lethal or mutagenic events (PLMEs) between DSBs in close proximity. Cell nucleus is simulated according to the chromosome territory-interchromatin compartment (CT-IC) model in that chromatin content is unevenly distributed in chromatin domains (CDs) and IC with a chromatin compaction ratio of 22:1. A particle track structure coordinate (PTSC) library was first generated for each particle type, energy, and dose based on a large number of particle track data obtained by running the Monte Carlo track structure code Geant4-DNA. To assess the DNA DSBs of a cell for a specific particle type, energy, and dose, the corresponding PTSC was selected and "map overlaid" onto 960 unique cell nucleus data sets containing chromatin fiber (CF) locations. Clustering algorithm DBSCAN was next used to identify the clustered energy deposition events occurring inside the CF. These events were then converted to DNA DSBs using a probabilistic approach. The locations of the DSBs thus obtained were, in turn, used to calculate PLMEs within the cell nucleus that can result from DSB proximity and complexity. The results obtained from this simulation study are correctly correlated to the experimental data of DSB yield and the RBE-LET relationships for various types of charged particles and of various energies. The results show agreement with other published radiobiological models.

## 1. Introduction

Earlier radiobiological models were predicated on microdosimetry, wherein the cell nucleus was considered the primary target for radiation damage [1]. Early imaging techniques were sufficient to show that damage to chromosome was closely related to radiation-induced cell death, as chromosome aberrations were visible under light microscopy [2]. The discovery of 2-nm diameter double helix structure of DNA in 1953 [3] along with the cell survival studies performed with the ultra-soft x-rays further suggested that double strand breaks (DSBs) of DNA are primarily responsible for chromosome aberrations and cell death [4,5]. Various radiation types were applied under different conditions, and cell survival curves were subsequently compiled showing variations in cell response with respect to absorbed dose, dose rate, LET, particle type, and cell type [6–10].

In addition to challenges posed by the physics processes involved in radiobiology, the discovery of higher-order structure in DNA is a recent discovery [11–13]. It was not until the early 2000's that advanced fluorescence tagging of individual chromosomes revealed each chromosome to occupy distinct chromosomal territories during interphase [14–16]. Further analysis revealed that each chromosomal territory was comprised of a multitude of chromatin domains (CDs) [16–18]. These CDs have a bead-like appearance and themselves are comprised of 30-nm-dia chromatin fiber (CF), while also containing approximately 1 million base pairs (Mbps) of DNA.

Due to limitations in technology and the complexities involved, early radiobiological models required major simplifications for practical application. Several models were hypothesized based on different mechanisms for action in observance of macroscopic experimental results [1,2]. It was proposed that neutrons cause cell death by single particle action while photon and electron radiation required dual radiation action [1]. While this approach was sensible, further work would reveal the importance of ionizing radiation's track structure on cellular response: experiments on mammalian cells involving aluminum

* Corresponding author.
*E-mail addresses:* brian.h.lee@northwestern.edu (B.H. Lee), chris.wang@nre.gatech.edu (C.-K.C. Wang).
[1] Present address.

https://doi.org/10.1016/j.ejmp.2019.05.006
Received 3 January 2019; Received in revised form 8 April 2019; Accepted 4 May 2019
Available online 21 May 2019

K-shell X-rays showed single low-energy electrons to be capable of causing cell death [4,19,20].

Among early simplifications still in common application is relative biological effectiveness (RBE), which is often the primary means of comparison for different particle types [10]. An earlier paper showed a unique relationship between RBE and the linear energy transfer (LET) of the radiation in that RBE increases with LET to a maximum at an LET of about 100 keV/μm and subsequently falls for higher LET values [21]. More recent studies, however, showed that the RBE-LET relationship varies for different ions with the tendency of heavier ions requiring higher LET for the same RBE than a lighter ion [22]. The current calculations of RBE do not account for enough factors to be practically applied [10,23–26]. Attempts have been made to apply the linear quadratic (LQ) model, which is widely used for low-LET radiation [27], to high-LET radiation [9,28–30]. The LQ model, however, is highly empirical and not comprehensive.

It is well known that radiation track structure and detailed DNA and chromatin organization have major implications on the biological effects of cells [31–38]. A comprehensive radiobiological model must include accurate simulation of particle tracks, water radiolysis simulation, and detailed subnuclear DNA and chromatin organization. Major advances have been made in the development of Monte Carlo simulations for radiobiology, notably Geant4-DNA [39–42] and PARTRAC [43], which were specifically developed for applications at the DNA and chromatin level. Detailed models have also been developed that incorporate structural features of DNA organization, extending to the molecular structure of DNA, nucleosome, and chromatin fiber [44,45].

Basic simplifications to track structure codes have been more recently applied with success in clinical and comparative applications. The MCDS code is based on the full particle track structure with an approximation of expected concentrations of DNA in the cell nucleus [46]. The Local Effect Model (LEM) is based on an amorphous track structure and a translation to DSBs, and while not simulating the full cellular DNA content, it has been validated for clinical applications [47]. Challenges with the amorphous track structure simplification is highlighted in the LEM extension GLOBLE for simulation of sparsely ionizing radiation types [48]. Prior work by Lee and Wang were largely based on similar assumptions using a single-track-effect simulation using heterochromatin fibers, but the need for the full cellular DNA content became evident as results deviated from the literature [49].

By directly incorporating an intermediate-complexity model of higher-order DNA conformation into a track structure code, spatial correlations of DNA damage should match results from molecular-detail codes while maintaining the computational efficiency required for a fast cell-by-cell simulation. In this paper, we present a cell-by-cell Monte Carlo simulation study that integrates Geant4-DNA and cell subnuclear structures to quantify DNA damage and proximity DNA DSB proximity for various types of radiation particle, energies, and absorbed doses.

## 2. Methods

The simulation study was divided into four independent parts: (1) creation of particle track structure coordinate (PTSC) library, (2) creation of cell nucleus data library, (3) production of DNA DSBs, and (4) evaluation of proximity between DSBs. Each of the four different parts uses different Monte Carlo algorithms and codes.

Fig. 1 is the flowchart showing how the four parts of simulation, as well as the additional details of each part, are put together to produce the final results. Each of the four parts produces its own “intermediate” results allowing the code to be validated against the results obtained from other methods, be it computational or experimental. The details for each of the four parts are elaborated in the subsections below.

### 2.1. Creation of particle track structure data library

The PTSC library was developed based on a large amount of PTSC obtained from running the Monte Carlo physics code Geant4-DNA (version 4.10.1.p02). The purpose of this was to run the computation-intensive Geant4-DNA calculation only once, and the acquired PTSC (stored in the coordinate library) can then be repeatedly fetched and “map overlaid” with the cell nucleus data to produce DNA DSBs on the cell-by-cell basis. Various types of particles (protons, carbon, helium, electrons, photons) were simulated at different energies. For electrons, an isotropic electron source was used by randomly producing electrons from outside of the cell nucleus with a randomized position and direction as shown in Fig. 2a. A beam-line approximation as shown in Fig. 2b was used in the production of the source particles (except for electrons), with all particles having up to a 0.087-radian divergence emanating from a uniform disc source larger than the cell nucleus, so as to appropriate in-scattered delta rays to compensate for out-scattered delta rays escaping from the cell nucleus. The intent for the divergence was to allow randomness in the trajectory of particle tracks while maintaining a primary direction, with the 0.087-radian value consistent with a 220-cm source-to-surface distance with a 20 cm treatment field width as may be used in a clinical scattered photon beam.

The PTSC library consists of a large number of data sets, of which each was identified via three parameters: particle type, initial energy, and absorbed dose. Each data set of the same dose, in turn, consists of 30 unique sets of PTSC, of which each corresponds to a different irradiation scheme. The purpose is to allow the additional randomness of particle track structure experienced by each cell nucleus for the cell-by-cell calculations. To assess radiation damage for a specific type of particle, initial energy, and dose, one of the 30 sets of PTSC was randomly selected using a random number generator. The particle track database contains information for every excitation and ionization event above 7-eV, including the x-, y-, and z- position in addition to the energy deposition and energy deposition type (i.e. excitation or ionization). 7-eV was assumed as a reasonable value due to being lower than the 8.22 eV electronic excitation threshold of liquid water [50]. To facilitate track structure analysis, the data of each particle track was further divided into two parts: those associated with the primary particle and those associated with the secondary electron. All simulations were performed using the default Geant4-DNA physics constructor, and tracking cuts were not used for low-energy electrons. Simulations for protons were performed with initial particle energies of 1-MeV, 3-MeV, 10-MeV, and 100-MeV. For helium-4 ions, simulations were performed at energies of 5-MeV, 20-MeV, and 400-MeV. Carbon-12 ion simulations were performed at 17-MeV/u, 185-MeV/u, and 290-MeV/u. Data was simulated for monoenergetic photons of 286-eV, 1.56-keV, and 28-keV to simulate carbon K-shell, and aluminum K-shell, and I-125 X-rays. Track structure data for electrons was performed with a uniformly distributed spectrum from 100-keV to 1-MeV. For all radiation types evaluated, PTSC data was produced at discrete mean doses of 0.5 Gy, 1.0 Gy, 2.0 Gy, and 4.0 Gy

As validation for Geant4-DNA, the stopping powers in liquid water for all charged particle types were compared with expected values obtained from the SRIM code [51]. Stopping powers for ions were calculated by tallying the kinetic energy loss of primary charged particles and dividing by the cord length within the cell nucleus for all tracks. The Geant4-DNA data was compared, and Table 1 shows these values do not match exactly but are in reasonable agreement. Since we have chosen to perform our analysis through the cross section libraries within Geant4-DNA, we matched the quantity of charged particles with the total energy loss simulated in Geant4. It is noted that the sum of individual energy depositions within cell nuclei from our output files is consistently 85% of the total energy lost by primary charged particles, which is due to a lower energy threshold of 7-eV to filter out events incapable of producing DNA damage. Dose confirmation was repeated by verifying the sum of events below the 7-eV threshold constitute 15%

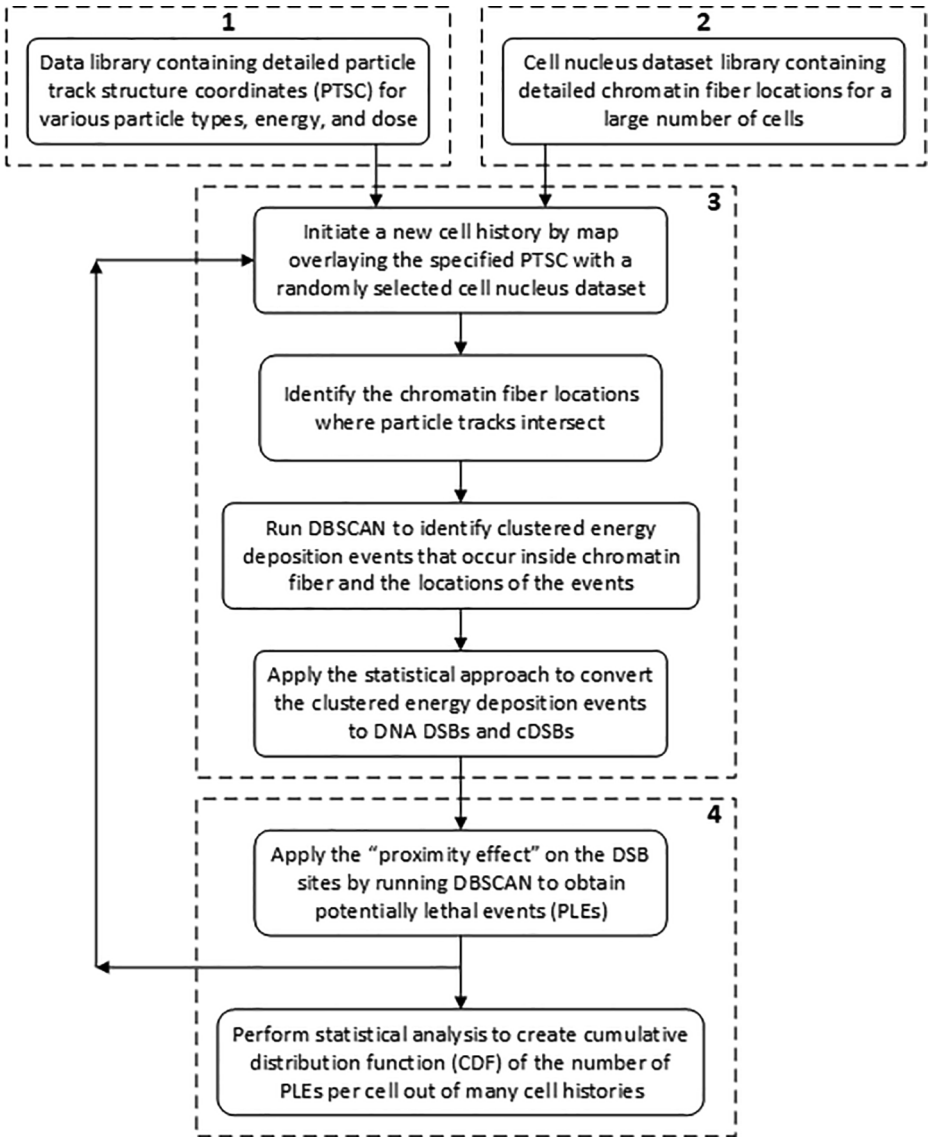


**Fig. 1.** The flowchart of the cell-by-cell Monte Carlo simulation for calculating radiation-induced DNA DSBs, DSB misrejoining events, and cell survival. The four independent parts of the simulation of are shown by the dotted boxes.

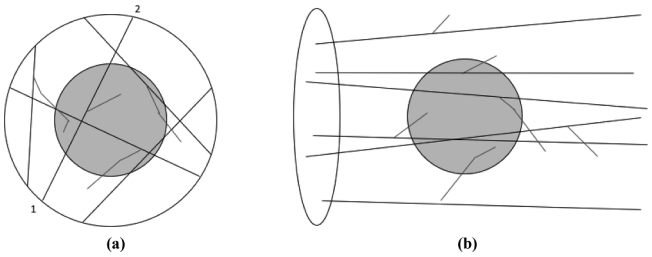


**Fig. 2.** (a) Isotropic electron source and (b) beam-line source. The electron source initiation is selected randomly at point 1 on the surface of a spherical volume larger than the diameter of the cell nucleus in the direction of a second randomly selected point 2, with electrons being produced until the total dose deposited within the cell nucleus is achieved. The beam-line source particles are initiated from a disk in the direction of the cell nucleus.

of primary particle kinetic energy losses.

Since electrons are capable of considerable deflection and transfer high proportions of their kinetic energy in hard collisions, it is not possible to determine dose from primary charged particle kinetic energy loss. Similar to the heavier charged particle dose consistency method, for electron and photon radiation the 85% ratio of energy deposition previously described was assumed to adjust the quantity of particle tracks and separately validated for low-energy events below threshold.

The simulation of tracks includes irradiation of a volume larger than the cell nucleus to produce conditions approximating charged-particle equilibrium (CPE). Delta rays escaping the cell nucleus are mostly compensated for by delta rays in-scattered from tracks adjacent to the cell nucleus. Since classically-defined CPE conditions are impractical to replicate at the scale of the cell nucleus, we compared the total kinetic energy losses of ions traversing the cell nucleus against the actual dose deposition which is within 8% for most of the particles simulated. Owing to the high kinetic energy of secondary electrons by 100-MeV protons and 400-MeV helium-4 ions, the proportion of secondary electron depositions is underestimated.

Direct radiochemistry simulations have largely been obviated in the current iteration of our model, although the influence of free radicals and indirect effects has effectively been incorporated through the clustered approach within the 30-nm diameter CF rod to be discussed with the DSB simulation. In the presented model, clustered excitation and ionization events occurring within a 30-nm diameter CF rod

**Table 1**
Comparison of the stopping powers obtained from SRIM and Geant4-DNA for various particle types and the corresponding value of the number of particle tracks per Gy.

| Particle type | topping power, keV/μm | | No. of tracks/ Gy (Geant4-DNA) | % Electronic equilibrium |
|---|---|---|---|---|
| | Geant4-DNA | SRIM | | |
| 1.0-MeV electron | | 0.20 | 2425 | |
| 1.56-keV photon | | | 5112 | |
| 286-eV photon | | | 16,285 | |
| 1.0-MeV proton* | 36 | 35.5 | 15.9 | 105.3% |
| 3.0-MeV proton | 12 | 12.1 | 48.7 | 102.1% |
| 10-MeV proton | 4.7 | 4.7 | 130 | 106.8% |
| 100-MeV proton | 0.72 | 0.74 | 1012 | 77.7% |
| 5-MeV He-4 ion** | 105 | 111 | 5.4 | 101.2% |
| 20-MeV He-4 ion | 29.7 | 32.6 | 19.9 | 105.8% |
| 400-MeV He-4 ion | 2.4 | 2.94 | 300 | 76.1% |
| 17 MeV/u C-12 ion | 99.4 | 111 | 6 | 100.6% |
| 185 MeV/u C-12 ion | 13.5 | 16.8 | 45.9 | 107.8% |
| 290 MeV/u C-12 ion | 10.3 | 12.7 | 61.8 | 104.6% |

* 1.0-MeV initial proton energy in the volume as modeled, average values at 0.6-MeV.

** 5.0-MeV initial helium ion energy in the volume as modeled, average values at 3.7-MeV.

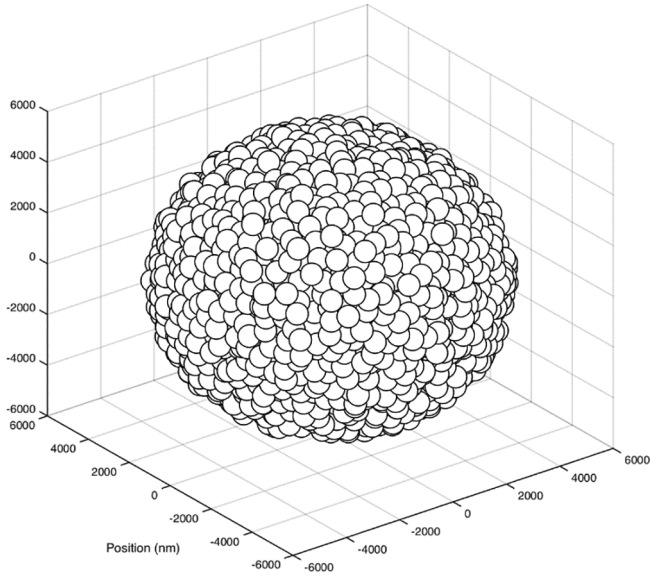


**Fig. 3.** The 3-D display of the cell nucleus model showing that the 400-nm diameter chromatin domains are randomly and uniformly distributed in the 11-μm diameter cell nucleus.

contribute to the probability of producing a DSB, either through direct damage to DNA or indirect damage through the production of free radicals within the volume encompassed by the CF rod. Several models in the literature have simulated direct effects for DNA damage by including excitation and ionization events in the DNA hydration shell, and subsequently accounting for indirect effects through a physicochemical stage several nanometers farther away from the point of DNA damage [43,52,53]. The assumption we took with our model is that by applying a stochastic approach to clustered damage within the 30-nm diameter CF rod, direct strand breaks and indirect damage by free radicals can be accounted for while not explicitly modeled. While ours is a substantial simplification, results from the DSB yield validation of this work indicate this approach still remains consistent with the literature.

### 2.2. Creation of cell nucleus data library

The data of a cell nucleus include the detailed information on where the DNA-containing chromatin fiber (CF) is distributed in the nucleus, and they are created based on the chromosome territory-interchromatin compartment (CT-IC) model [14,16,17]. The model divides the cell nuclear volume into two regions: the chromatin dense region, and the chromatin sparse region. The former comprises a large number of spherical chromatin domains (CDs) which are dense in CF. The latter is referred to as the interchromatin compartment (IC), which encompasses the space between the CDs and is sparse in CF. Specifically, the cell nucleus is modeled as an 11-μm diameter sphere consisting of the coordinates (i.e. positions) of the detailed "subnuclear structures": CF, CD, and IC, from which the PTSC can be used to overlay and produce DNA DSBs. The CF is modeled in its extended form of 30-nm in diameter. Each CD is modeled as a sphere of 400 nm in diameter, and it is made of a cluster of CF containing approximately 1 Mbps of DNA [17,34]. The total quantity of DNA within a human cell nucleus is assumed to be 6 Gbps [54]. As such, the code is assembled such that the cell nucleus contains approximately 6000 CDs as can be seen in Fig. 3. The total volume and DNA content of the cell nucleus has been modeled after the human fibroblast cell as is used in other prominent track structure publications [52,55].

While in a real cell nucleus CF is a continuous piece of strand, in our model the CF is broken into many discrete pieces of "rod" so that they can physically fit into the discrete CDs. Each CF rod is a cylinder 30-nm in diameter and 150-nm long. It corresponds to approximately 18 kilobase pairs (kbps) of DNA [31]. Accordingly, a CD containing 1 Mbps of DNA would contain 56 CF rods. However, to offset the amount of CF located within the IC, the genome content of 1 Mbps in each CD was reduced accordingly. The literature indicates that the compaction of genome in CDs is at least 10 times higher than that in the IC [17]. In our model, we assumed the compaction rate of CF rods at a ratio of 22:1 between the CDs and the IC. Given that CDs in our model occupy 29% of the cell nucleus, and the IC occupies 71% of the cell nucleus, the relative compaction ratio would place about 90% of the CF within CDs and 10% in the IC. This also means that each CD contains 50 CF rods (or 0.9 Mbps).

Fig. 4 shows the general layout of the subnuclear structures: CDs, IC, and CF rods, with a charged particle track randomly intersecting these structures. As shown, the CF rod density is significantly higher within CDs than in the IC. One obvious indication of this model is that the majority of energy deposition by ionizing radiation causes no DNA damage. This is because the majority of the energy deposition events along a particle track are in the CD and the IC regions that are devoid of CF rods. Only a very small subset of energy deposition along a particle track intersects CF rods, and of the energy deposited to CF rods an even smaller proportion will lead to DNA DSBs.

The detailed procedures are described in subsection 2.2.1–2.2.3 below. The cell nucleus data library used in this study includes 960 individual sets of cell nucleus data, allowing additional randomness of CF distribution in a cell nucleus for the cell-by-cell calculations.

#### 2.2.1. Sphere packing algorithm for CD placement

A code was written to pack 6000 CDs of 400-nm diameter each into the spherical cell nucleus of 11-μm in diameter as can be seen Fig. 3. It is based on a stochastic approach dividing the cell nucleus between an IC and a multitude of CDs. None of the CDs are intersecting with each other, and the IC is simply defined as the region of the cell nucleus devoid of CDs. A library of 150 CD conformations was produced, from which the CD pattern is selected by a RNG value for each individual cell.

A cubic volume of lengths of 11-μm is defined, and a uniform random number generator populates the cartesian coordinates of points within the cube. A new point is stochastically placed and verified to be no closer than 400-nm to any other previously generated point within the cubic volume. Once all points are positioned within the cubic volume, only points within a 5.5-μm radial distance from the center are kept. In this manner, only the CDs that can be fully contained within an

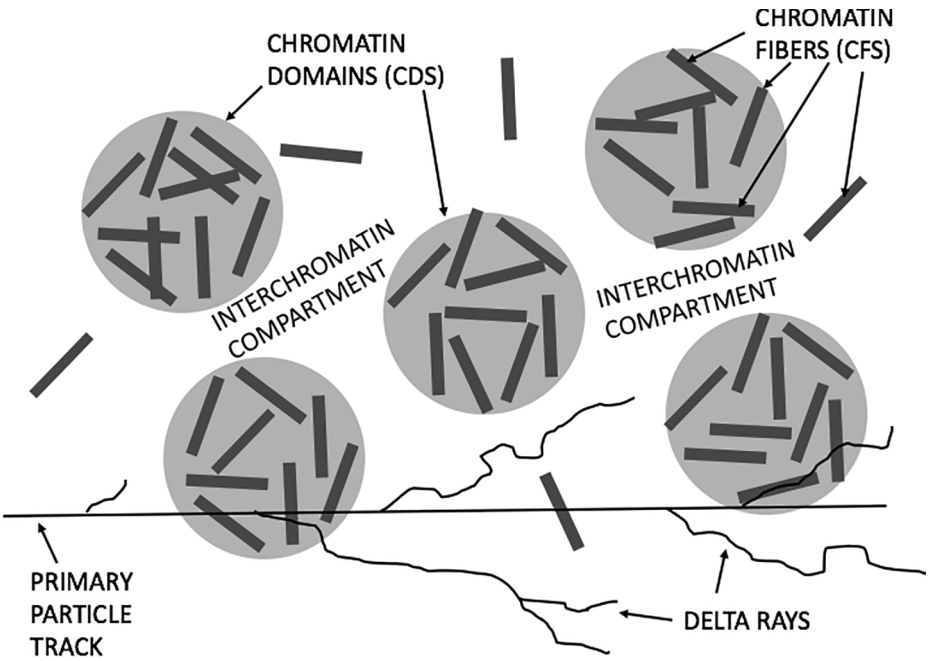


**Fig. 4.** The layout of the subnuclear components: CDs, IC, and CF rods, with a charged particle track randomly intersecting these structures.

11-μm diameter cell nucleus are kept. The center points of the first 6000 CDs produced by the RNG method are tallied.

*2.2.2. Placement of CF rods*

The placement of the CF rods in 3-D space inside the cell nucleus was based on the 1-D mean-free-path (MFP) approach. The idea was inspired from the "random walk" procedure used in the Monte Carlo method to randomly determine the distance to the next collision point in neutron/photon transport calculations [56]. If one considers a straight line traversing the cell nucleus, the distance for the line to encounter (or intersect) a CF rod can be determined by:

$$S = -\lambda \ln \Re \tag{1}$$

where $\Re$ is a random number having a value between 0 and 1, and λ is the MFP for the line to intersect a CF rod. It has been shown that λ is simply the inverse of the "macroscopic cross section (Σ)" of the CF rods in the medium, where Σ can be calculated as:

$$\Sigma = N\sigma \tag{2}$$

where $N$ is the number density of the CF rods in the medium and it has the unit of CF rods $\mu m^{-3}$, and $\sigma$ is the geometric cross section of each CF rod and it has the unit of $\mu m^2$ per CF rod. Accordingly, Σ and λ have the unit of $\mu m^{-1}$ and μm, respectively.

To apply the Monte Carlo procedure of Eq. (1), one first calculates $\sigma$ of a CF rod. Because we assume the CF rod orientations are random and isotropic, $\sigma$ of the cylindrical CF rod should be equivalent to that of a sphere having the same volume. Given a 30-nm cylindrical diameter and a 150-nm length, the sphere radius can be obtained by solving the equation:

$$\frac{4}{3}\pi r^3 = \pi(15\text{ nm})^2(150\text{ nm})$$

which yields $r \cong 29.36$ nm. The "sphere-equivalent" cross section of a CF rod is then obtained as:

$$\sigma = \pi(0.02936\ \ \mu m)^2 \cong 0.00271\ \mu m^2 \text{ per CF rod}$$

Since each CD contains 50 CF rods, the number density of CF rods in a CD is calculated as:

$$N = \frac{50 \text{ CF rods}}{\frac{4}{3}\pi(0.2\ \mu m)^3} = \frac{50 \text{ CF rods}}{0.03351\ \mu m^3} \cong 1492\ \ \text{CF rods}\ \mu m^{-3}$$

The values Σ and λ in each CD can be calculated, respectively, as:

$$\Sigma = N\sigma = (1492\ \mu m^{-3})(0.00271\ \mu m^2\ \text{CF rod}^{-1}) \cong 4.04\ \mu m^{-1}$$

and

$$\lambda = \frac{1}{\Sigma} = \frac{1}{4.04\ \mu m^{-1}} = 0.248\ \ \mu m = 248\text{ nm}$$

Similarly, one can calculate the number density of CF rods in the IC and obtain the corresponding values of Σ and λ to be 0.182-$\mu m^{-1}$ and 5.49-μm, respectively. Once the values of Σ and λ in CDs and IC are determined, one can then apply Eq. (1) to determine $S$ along a straight line traversing the cell nucleus to randomly placing a CF rod inside the cell nucleus. This procedure is repeated as until the total number CF rods (a total of 333,333) are placed.

The above procedure was implemented via a 3D grid of parallel lines traversing the cell nucleus as shown in Fig. 5. The parallel lines allow for the 1D-MFP to be correlated to Cartesian coordinates. Using the values of λ and given that 90% and 10% of the CF rods are located in the CDs and IC, respectively, one calculates a total chord length of 256,666 μm in order to place all CF rods in the cell nucleus. The total number of parallel lines was then obtained by dividing 256,666 μm with the 7.333-μm mean chord length of the cell nucleus to be 35,000.

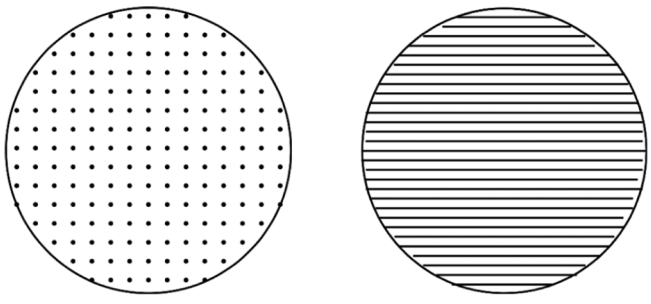


**Fig. 5.** Grid of parallel lines. (a) cross section showing grid pattern of lines, (b) a side view showing lines traversing the entire cell nucleus.

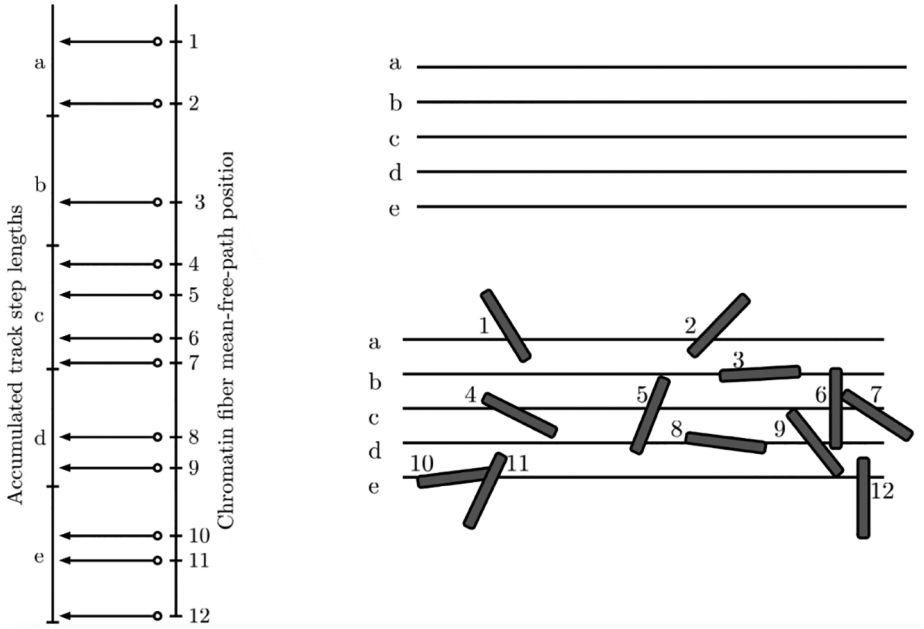


**Fig. 6.** The MFP approach along a fixed grid of parallel lines in determining the positions of CF rods. The pathlengths of the lines are aligned as one leg of a ladder. The intersection points based on the MFP are aligned as the second leg of a ladder. CF rods are positioned at the intersections with predetermined orientations.

That is, by using a grid of 35,000 equally spaced parallel lines traversing the cell nucleus, one is able to randomly place all CF rods in the CDs and IC according to the specified CF compaction ratio of 22:1. Fig. 6 shows the method by which a MFP distance between CF rods is applied to the parallel lines, and the method is shown to be analogous to rungs of a ladder.

The parallel lines traversing the cell nucleus are “unfolded” and aligned sequentially in 1D like the left leg of a ladder as shown in Fig. 6. The MFP positions of CF rods are similarly aligned as the right leg of the ladder. Each CF rod start position based on the 1D MFP is matched as the rung of a ladder to a position matching the parallel lines on the left leg of the ladder in Fig. 6. When the parallel lines are “folded” back to their corresponding positions in the 3D space of the cell nucleus, the CF rods will similarly be positioned at a specific 3D coordinate in the cell nucleus.

To account for different densities of CF rods in CDs and the IC, the parallel lines are separated between segments occurring in the CDs versus in the IC. For segments in the IC, a longer MFP is used to account for the lower density of CF rods, while in the CD a shorter MFP is applied.

Owing to the stochastic placement of CF rods in the presented model, overlap of CF rods is permitted. While CF rod overlap is not excluded in the model, energy depositions to CF rods by charged particles are assigned to a single CF rod and hence will contribute to DNA damage only once. Since the CF rod density and quantity translates to occupying 4% of the volume of the cell nucleus, it can be deduced that 4% of the total volume of CF rod can be expected to overlap within the cell nucleus as modeled and hence the volume of DNA accounted for is slightly underestimated.

### 2.2.3. Orientation of CF rods

Once the starting position of the CF rod is determined from the intersection point along the parallel line, offsets and rotations are applied to the CF rod. Fig. 7 shows the geometric orientation of a CF rod with respect to an intersecting line. The orientation is determined based on two direction vectors, $\vec{\Omega}$ and $\vec{\Omega}'$. The vector $\vec{\Omega}$ is determined by two points, the track entry point, $(x_1, y_1, z_1)$, and the center point of the CF rod, $(x_2, y_2, z_2)$. The direction cosines of $\vec{\Omega}$ (i.e. $u$, $\upsilon$, and $w$) are determined by a set of Monte Carlo procedures that provides random and

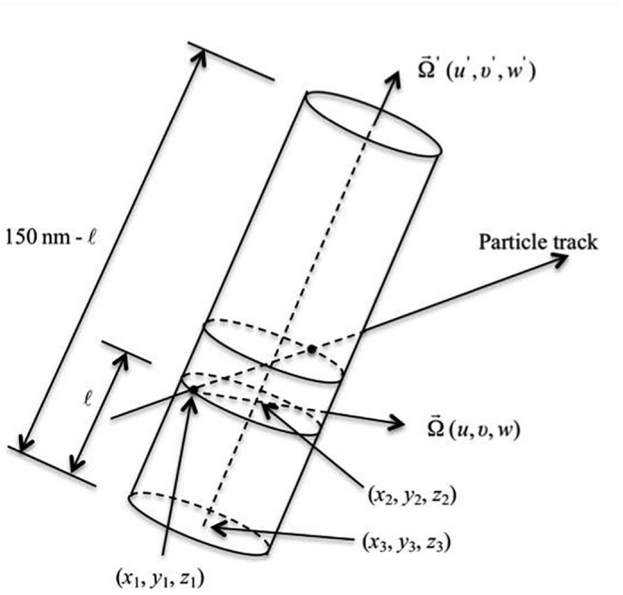


**Fig. 7.** The geometric orientation of a CF rod with respect to the particle track intersecting it.

isotropic selection of a direction vector [56]. After $u$, $\upsilon$, and $w$ have been determined, the direction cosines of $\vec{\Omega}'$ (i.e. $u'$, $\upsilon'$, and $w'$) are obtained via the following relationships [57]:

$$u' = u\cos\theta + (uw\cos\varphi - \upsilon\sin\varphi)\left(\frac{\sin\theta}{\sqrt{1-w^2}}\right) \quad (3)$$

$$\upsilon' = \upsilon\cos\theta + (\upsilon w\cos\varphi + u\sin\varphi)\left(\frac{\sin\theta}{\sqrt{1-w^2}}\right) \quad (4)$$

$$w' = w\cos\theta - \cos\varphi\sqrt{1-\cos^2\theta}\sqrt{1-w^2} \quad (5)$$

where $\phi$ and $\theta$ are, respectively, the azimuthal angle and polar angle used to describe the directional relationship between two arbitrary

direction vectors in the polar coordinate. Because $\vec{\Omega}$ and $\vec{\Omega}'$ are perpendicular to each other (i.e.$\theta$=90°), Eqs. (3)–(5) are reduced to:

$$u' = \frac{uw\cos\varphi - v\sin\varphi}{\sqrt{1-w^2}} \quad (6)$$

$$v' = \frac{vw\cos\varphi + u\sin\varphi}{\sqrt{1-w^2}} \quad (7)$$

$$w' = -\cos\varphi\sqrt{1-w^2} \quad (8)$$

The endpoints of the CF rod is defined by three parameters, the center of the base, ($x_3$, $y_3$, $z_3$), the direction vector of its axis, $\vec{\Omega}'(u', v', w')$, and the total length of the CF rod, which is 150-nm. Because the distances between ($x_2$, $y_2$, $z_2$) and ($x_3$, $y_3$, $z_3$) varies arbitrarily between 0 and 150-nm, $x_3$, $y_3$, and $z_3$, can be obtained as:

$$x_3 = x_2 - u'\ell \quad (9)$$

$$y_3 = y_2 - v'\ell \quad (10)$$

$$z_3 = z_2 - w'\ell \quad (11)$$

where $\ell$ = (150 mn)·$\Re$, of which $\Re$ is a random number between 0 and 1.

### 2.3. Production of DNA double strand breaks (DSBs)

As shown in Fig. 1, the first step in simulating DNA DSBs is to initiate a cell history by fetching one set of data from each library and then do the "map overlay". Each CF rod is treated as an independent detector region. Any energy transfer events of the PTSC that intersect the CF rods are identified by CF rod and sorted out from those that do not intersect the CF rods, which are ignored.

The DBSCAN clustering algorithm [58,59] is applied to the radiation events contained within each individual CF rod to find clustered events that may lead to DNA DSBs. A 2-nm radial distance (which is based on the diameter of the DNA double-helix) and a minimum of 2 events are used as the cluster parameters in DBSCAN to produce "energy clusters" for further analysis [60]. Sparse events occurring within CF rods are thus excluded. When multiple clusters are formed within a CF rod, the total energy from all clusters is used to assess the likelihood of DSB production.

The clustering approach to cylindrical volumes was utilized in part to incorporate the influence of hydroxyl radical formation and indirect damage to DNA. The CF rods that are the primary target in our model are largely comprised of water and histone proteins, and free radical production is expected within the energy depositions to the CF rods. While the migration of free radicals is not explicitly modeled, the radial distance of 2-nm defining excitation and ionization events within a cluster includes both direct and indirect DNA damage within the CF rods. This is consistent with models that tally energy depositions within the hydration shell as leading to SSBs by direct effect [52,53].

The likelihood of an energy cluster to produce a DSB is determined by a statistical approach. It uses a cluster threshold of 75-eV as the step size and a random number to obtain the probability of producing a DSB. The 75-eV threshold adapted from the previously-reported quasi-threshold of 100-eV deposited to the double-helix for DSB induction, in conjunction with experimental observation that depositions between 25 and 50-eV are sufficient for producing DSBs [61]. Calibration of the probability of producing 40–50 DSB's $Gy^{-1}$ of electron radiation yields a 10% likelihood of a 75-eV cluster producing a DSB [60]. The small likelihood is consistent with the fact that only a small percentage of the CF is occupied by DNA. To implement the Monte Carlo procedure, the RNG is called once for a 75-eV cluster, twice for a 150-eV cluster, etc. Since the chance for a 75-eV cluster not to produce a DSB is 90%, the chance for a 150-eV energy cluster to produce a DSB would be 1-$(0.90)^2 \cong$ 19.0%, and that for a 225-eV energy cluster would be 1-$(0.90)^3 \cong$ 27.1%, etc. The above approach presumes that the spatial distribution of DNA inside a chromatin fiber is uniform. Hence, larger energy clusters have a higher likelihood of producing DNA DSBs while still accounting for uncertainties in the composition of chromatin structures.

Energy clusters wherein a single value meets the threshold criteria are counted as normal double-strand breaks (DSBs), while clusters where multiple RNG values meet the threshold are counted as complex double-strand breaks (cDSBs). It is important to note that the definition of cDSBs as applied in this work differs from the scoring methods applied in more detailed models [45,52,53], as individual base damage and strand breaks are not directly simulated. Rather, the tally of multiple RNG values meeting threshold are simply referred to as cDSB and encompasses spectrum of multiply-damaged DNA DSBs and clusters of DSBs in near proximity within the same CF rod [60]. Clusters not meeting criteria as DSBs are tallied separately but currently ignored.

### 2.4. Proximity effect of DSBs and potentially lethal or mutagenic events (PLMEs)

As shown in Fig. 1, the next step of the simulation is to analyze data associated with the spatially distributed DSBs in each cell nucleus. The simulation employs the concept of "proximity effect" [62], which describes how free ends of DSBs interact with one another. While a single isolated DSB can produce lethal chromosome aberrations and cell death, the chief mechanism of cell death involves the interactions of two or more DSBs initially in close proximity.

To implement the proximity effect, each cell nucleus simulation identifies the DSB clusters by running the spatially distributed DSBs through DBSCAN clustering algorithm with the distance parameter of 1-μm. In other words, DSBs located less than 1-μm from one another are identified and included as a DSB cluster; and only the DSBs within a cluster are allowed to interact with other DNA DSBs. The distance of 1-μm is also known as the "proximity parameter", a nominal value drawn from the previous experimental observations and simulation studies [34,62–67].

To assess potentially lethal or mutagenic events (PLMEs), the DSB clusters identified in each cell are further categorized based on the surroundings of the DSBs involved. For example, some clusters may contain DSBs from the same CD, others contain DSBs from different CDs, and still others contain DSBs from CF rods located in the IC as shown in Fig. 8. Incidences of DSBs occurring within the same CD can contribute to the formation of micronuclei if misrejoined, while DSBs involving CF rods within the IC will have a higher likelihood of producing chromosomal aberrations. Hence, each DSB cluster has a set of data including the number of CF rods involved and their originating cell nucleus structures.

The central assumption is that interaction of DSBs could lead to a PLME. A clustering algorithm applied to DNA DSBs is a logical approach to chromosome aberration modeling: nearby DSBs have some probability to misrejoin. Similarly, increasing the number of DSBs in a cluster proportionally increases the probability of PLMEs.

In the case of two DSBs in proximity, a single PLME is tallied due to this type of misrejoining being the simplest form possible. Where three or more DSBs are clustered together, the number of DSBs in the cluster is counted as the number of PLMEs. Consideration for larger DSB clusters reveals the logic behind this approach: as the number of DSBs in a cluster increases (e.g., 5 DSBs), the restitution possibilities increase dramatically beyond any sensible, experimentally observed pattern.

In cases where multiple CF rods in a CD tally DSBs, the CD is noted for potential micronucleus formation. Since DSBs to CF rods within a CD are more spatially restricted, misrejoining of DSBs within the same CD are likely to cause a loss of a small segment of DNA or micronucleus formation, but unlikely to form an exchange-type chromosomal aberration. Consequently, for the DSB clustering calculations, we only count a single DSB from the CD but note when multiple DSBs are tallied

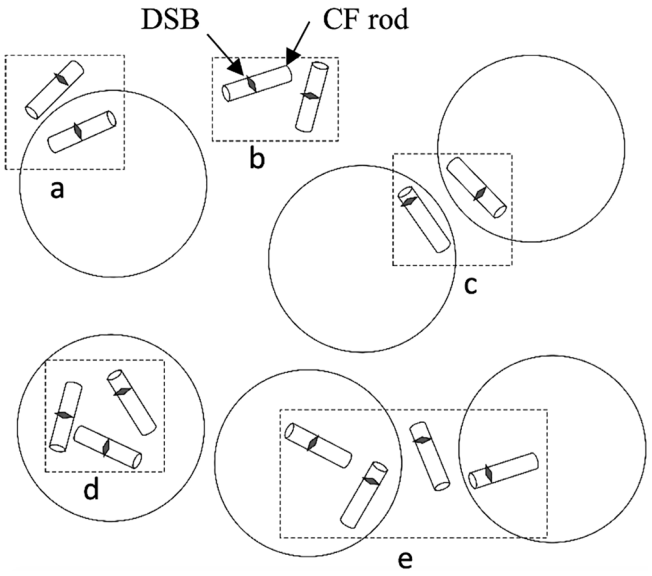


**Fig. 8.** Categories of DSB clusters. a, b, and c are simple misrejoining events between two DSBs in different CF rods and each counted as one potentially lethal or mutagenic event (PLME). (d) shows a 3 DSBs in the same CD which is counted as possibly yielding one micronucleus and a single PLME, (e) shows a complex interaction involving two distinct CDs and one IC CF rod, counted as one possible micronucleus and three misrejoining options as a total of 4 PLMEs.

within the CD.

## 3. Results

Table 2 shows the projected yields of DSBs and cDSBs. As shown, the number of DSBs produced are in the expected range for most types, and the escalated yield of DSBs for the high-LET 5-MeV helium ions and 17-MeV/u carbon ions relative to 1.0-MeV electrons match reported results from other radiobiological models.

DSB yield comparisons are shown in Fig. 9, and show our model's DSB simulation applied to Geant4-DNA to be in good agreement with several models in the literature. Our results are also plotted with cDSBs being counted as two DSBs as this is more consistent with reporting methods utilized by molecular-detail codes.

Our DSB yields are noted to agree very well with results published by Stewart in MCDS [46]. This is likely due to both models utilizing the Monte Carlo method and clustering for simulating DSBs. DSB yields from proton simulations follow the same trend as published results of Geant4-DNA, with the ratio of DSB/cDSB yields from our model shown to be consistent in relative proportion [52].

Proportions using Geant4-DNA for a separate MCTS simulation shows values calculated for electron calculations with our reference 1.0-MeV electron spectrum compared to their 220-keV electron simulation [68]. The calibrated values for DSB yields is smaller than our results, indicating a difference in calibration parameters; however, the ratio of DSB yields between electron energies is similar to our results.

**Table 2**
DSB Yields.

| Particle type | No. of DSBs/Gy | No. of cDSBs/Gy |
|---|---|---|
| 1.0-MeV electron | 42.3 ± 6.7 | 2.3 ± 1.5 |
| 1.56-keV photon | 83.9 ± 9.3 | 6.1 ± 2.5 |
| 286-eV photon | 99.6 ± 9.6 | 5.0 ± 2.2 |
| 1.0-MeV proton | 94.3 ± 15.3 | 12.6 ± 3.9 |
| 3.0-MeV proton | 67.2 ± 9.2 | 3.8 ± 2.0 |
| 10-MeV proton | 52.6 ± 7.7 | 2.8 ± 1.7 |
| 100-MeV proton | 44.5 ± 6.6 | 2.4 ± 1.5 |
| 5-MeV He-4 ion | 67.0 ± 14.7 | 31.8 ± 8.1 |
| 20-MeV He-4 ion | 85.9 ± 12.9 | 6.7 ± 2.8 |
| 400-MeV He-4 ion | 44.2 ± 7.0 | 2.5 ± 1.6 |
| 17-MeV/u C-12 ion | 69.6 ± 13.9 | 16.9 ± 5.1 |
| 185-MeV/u C-12 ion | 61.7 ± 8.9 | 3.4 ± 1.9 |
| 290-MeV/u C-12 ion | 55.8 ± 7.9 | 2.9 ± 1.7 |

Our DSB yields with double-counted cDSBs are in reasonable agreement with results from PARTRAC/KURBUC [53]. There are distinct differences in how DSBs are tallied between the codes: PARTRAC tallies DSBs as independent when distances exceed 25 bp (~8.5 nm), DSB clusters as multiple DSBs separated by less than 25 bp and DSB sites as the sum of DSB clusters and individual DSBs, whereas our model denotes cDSBs for multiple DSBs tallied within the same CF rod of 30-nm diameter. Accounting for this, our DSB yields are in a reasonable range for helium and carbon ions, although our yields are notably higher for protons. Fig. 10 shows the yields of cDSBs as defined in our work with the DSB cluster yield as published in PARTRAC [53]. The cDSB yields from our code are noted to be significantly larger, but by a consistent factor than the DSB clusters in PARTRAC/KURBUC. Hence, it may be possible to apply an RNG to our model's cDSB yields to replicate the DSB cluster yields of a molecular detail DNA model (i.e., 4% of cDSBs in our model translating to DSB clusters).

Experimental results of the RBE of DSB yield are shown in Table 3 for particle types and energies with experimental values of similar LET and radiation type reported in the literature [69–73]. Experimental RBE's are listed with the reference radiation type, while RBE results from this workare compared against simulated 1.0-MeV electron radiation, with good agreement observed for photon and proton radiation types [69–72]. Patterns observed for helium-4 and carbon-12 ions are seen to be in excess of experimental results [70–73].

PLMEs are shown in Fig. 11 at different doses for 1.0-MeV protons. A large variability is noted in the number of expected DSBs in proximity even at consistent dose. Of particular note is the overlap of expected PLMEs seen in broadly different doses. This is of consequence when assessing cell survival parameters, as simplifying assumptions regarding a uniform 40 DSB per Gy or any other basic parameter is noted to be problematic.

Fig. 12a shows a histogram of the number of PLMEs per cell for 4 Gy of 1-MeV electron irradiation based on results obtained from simulating 960 cells. PLMEs per cell for this irradiation scheme approximately follows a normal distribution. Fig. 12b shows the CDF derived from Fig. 12a, which we propose as consistent for applications using Monte Carlo first principles.

The rationale behind assessing PLMEs per cell is to establish a framework by which a simplified statistical approach to cell survival can be investigated for future work. Additional details to validate such a predictive approach is currently beyond the scope of this work: rather, we present the statistical variance in PLMEs per cell as observed from this study to indicate that gross simplifications common to RBE comparisons merit such an approach to be investigated.

## 4. Discussion

The most important results of this study are the validation of the yields of DNA DSBs in a cell nucleus for the various radiation types. These results were calculated on the cell-by-cell basis, and are unique for each specified irradiation conditions including radiation type, energy, dose … etc. The pattern of DSB yields shown in Tables 2 & 3 and Fig. 9 are consistent with the previously published results [46,52,53,68–73]. This consistency serves as a validation for parts (1), (2), and (3) of the simulation study (i.e. Fig. 1).

It is important to reiterate the presented model is of an intermediate-complexity, with the overall intent to provide a novel tool by which studies in radiobiology can be accelerated. This presents with several shortcomings in comparison to more sophisticated and computationally intensive models [53,74], including the lack of direct simulation of radiochemistry and non-inclusion of a molecular-detail

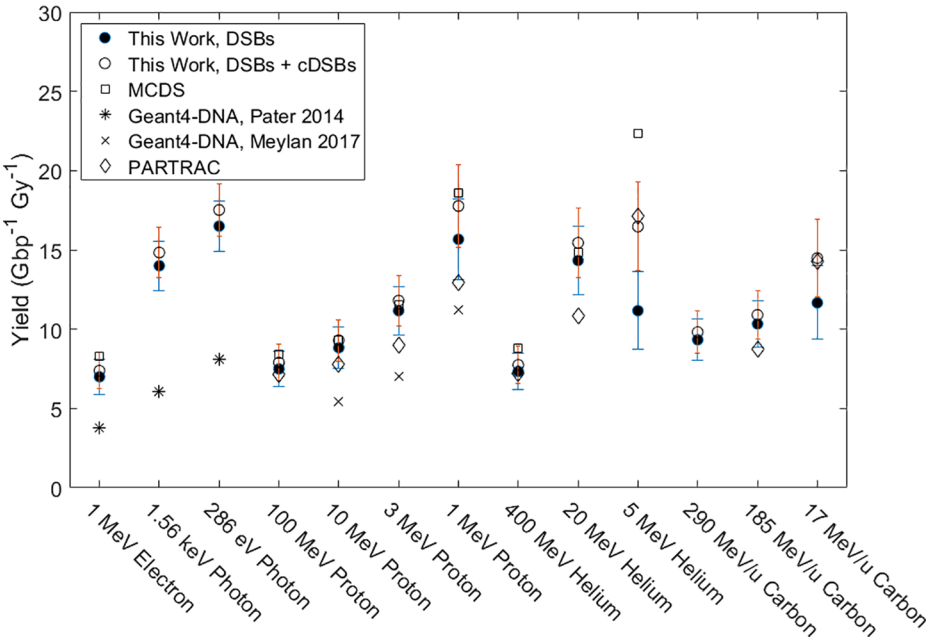


**Fig. 9.** DSB yield comparison of model results to other simulations. Filled circles represent all DSBs and cDSBs, open circles reflect DSBs with individual cDSBs counted as two DSBs. Open squares represent results from the MCDS code [46], asterisks represent Geant4-DNA results for reference photon and ultrasoft X-ray irradiation [52], x's represent Geant4-DNA results for protons [68], and diamonds represent PARTRAC results [53].

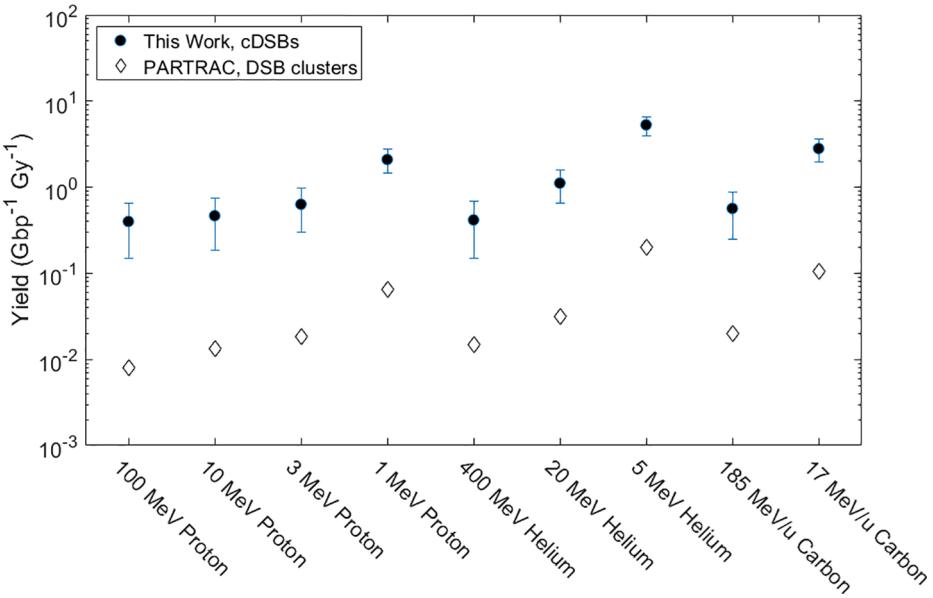


**Fig. 10.** cDSB yield of model compared to PARTRAC DSB cluster simulation [53].

DNA model. The most obvious areas lacking are that a direct scoring of strand breaks, base damage, and degrees of complexity as detailed by other authors [45,52,53], is not feasible with the presented model, and simulating the diffusion of free radicals is of limited value owing to lack of fine resolution DNA structures. However, inclusion of the full DNA content with a CT-IC model of chromatin fibers provides a level of sophistication that can still provide valuable insights while applying track structure modeling.

The DSB yields from our model applied to Geant4-DNA are in on a similar order of results as published from models incorporating sophisticated nanoscale DNA geometry. Some variations are present owing to differences in definitions and scoring compared to other radiobiological models in the literature. What is of particular note is that the presented model, even with simplifications, remains consistent in the overall yield of DNA DSBs without requiring correction factors for differences in radiation types or quantities. This is a benefit that proves challenging for analytical radiobiological models [48,75]. This shows that the presented model can be correlated to more complex, molecular-detail models accurately. Additional work is needed to more thoroughly correlate the resulting cDSBs produced in this work to more complex damages as reported in PARTRAC, Geant4-DNA, and other authors [45,52,53,75].

The most novel portion of work is seen in the number of PLMEs in Figs. 11 and 12, which vary substantially for the same particle type and dose across the 960 cell irradiations simulated, and the statistically consistent pattern indicates that a Monte Carlo approach to spatial patterns of DNA DSBs within the cell nucleus may be appropriate. In conjunction with the presented model's ability to distinguish differences in the categories of clusters of DSBs, relevant biological parameters and cell killing mechanisms may be correlated through the presented statistical methods for producing simulated cell survival curves, estimating DNA fragment sizes, and chromosomal aberration yields.

Additional work is needed to estimate DNA fragment sizes based on

**Table 3**
RBE of DSB yields compared to experimental results in mammalian cells.

| | LET (keV/um) | RBE of DSB yield | Reference | Source |
|---|---|---|---|---|
| 1.56-keV photon | | 2.0 ± 0.27 | 1.0-MeV electrons | this work |
| Al-K X-Rays | | 1.9 | Co-60 gamma rays | DeLara et al. [69] |
| 286-eV photon | | 2.4 ± 0.28 | 1.0-MeV electrons | this work |
| C-K X-Rays | | 2.7 | Co-60 gamma rays | DeLara et al. [69] |
| Protons | 36 | 2.2 ± 0.39 | 1.0-MeV electrons | this work |
| Protons | 35 | 2.0 | 15-MeV electrons | Frankenberg et al. [70] |
| Protons | 31 | 1.9 ± 0.1 | Co-60 gamma rays | Belli et al. [71] |
| Protons | 23 | 1.4 | 15-MeV electrons | Frankenberg et al. [70] |
| Protons | 12 | 1.6 ± 0.27 | 1.0-MeV electrons | this work |
| Protons | 10.9 | 1.2 ± 0.08 | Co-60 gamma rays | Belli et al. [72] |
| Protons | 7.9 | 1.4 | 15-MeV electrons | Frankenberg et al. [70] |
| Protons | 4.7 | 1.2 ± 0.24 | 1.0-MeV electrons | this work |
| Helium-4 | 124 | 1.2 | 15-MeV electrons | Frankenberg et al. [70] |
| Helium-4 | 123 | 1.2 ± 0.1 | Co-60 gamma rays | Belli et al. [71] |
| Helium-4 | 105 | 1.6 ± 0.38 | 1.0-MeV electrons | this work |
| Helium-4 | 35 | 1.4 | 15-MeV electrons | Frankenberg et al. [70] |
| Helium-4 | 29.7 | 2.0 ± 0.34 | 1.0-MeV electrons | this work |
| Helium-4 | 27 | 1.3 | 15-MeV electrons | Frankenberg et al. 1999 [70] |
| Carbon-12 | 103 | 1.0 | 250-kVp X-rays | Heilmann et al. [73] |
| Carbon-12 | 99.4 | 1.6 ± 0.36 | 1.0-MeV electrons | this work |
| Carbon-12 | 14 | 1.0 | 250-kVp X-rays | Heilmann et al. [73] |
| Carbon-12 | 13.5 | 1.5 ± 0.26 | 1.0-MeV electrons | this work |

PLMEs: since the chromatin model is stochastic and non-contiguous, an appropriate method for approximating the CF rods into a quasi-sequential pattern would have to be developed. Additional factors incorporated into the model include the definition of chromosome territories by stochastic allocation of regions of the cell nucleus [60], which require additional validation and can provide a means of differentiating PLMEs within one chromosome to those involving multiple chromosomes. Hence, the CT-IC model used for placement of CF rods should readily translate to estimations of complex chromosome aberration yields for PLMEs occurring in different chromosomes and micronucleus formation for DSBs tallied within the same CD. Translation of PLMEs to cell survival curves necessitates a rigorous review of the literature, but a successful comparison of PLMEs to cellular endpoints would enable future correlations to analytical or amorphous track structure codes, such as the RKM, MK, and LEM models [75–77].

One may also think of using the presented model to evaluate the radiation weighting factors for radiation protection purposes. This can be done by straightforwardly establishing the PTSC for various radiation types of very low dose levels, e.g. 1 mGy. The issue of statistical uncertainty, however, necessarily arises because the DSB yield becomes

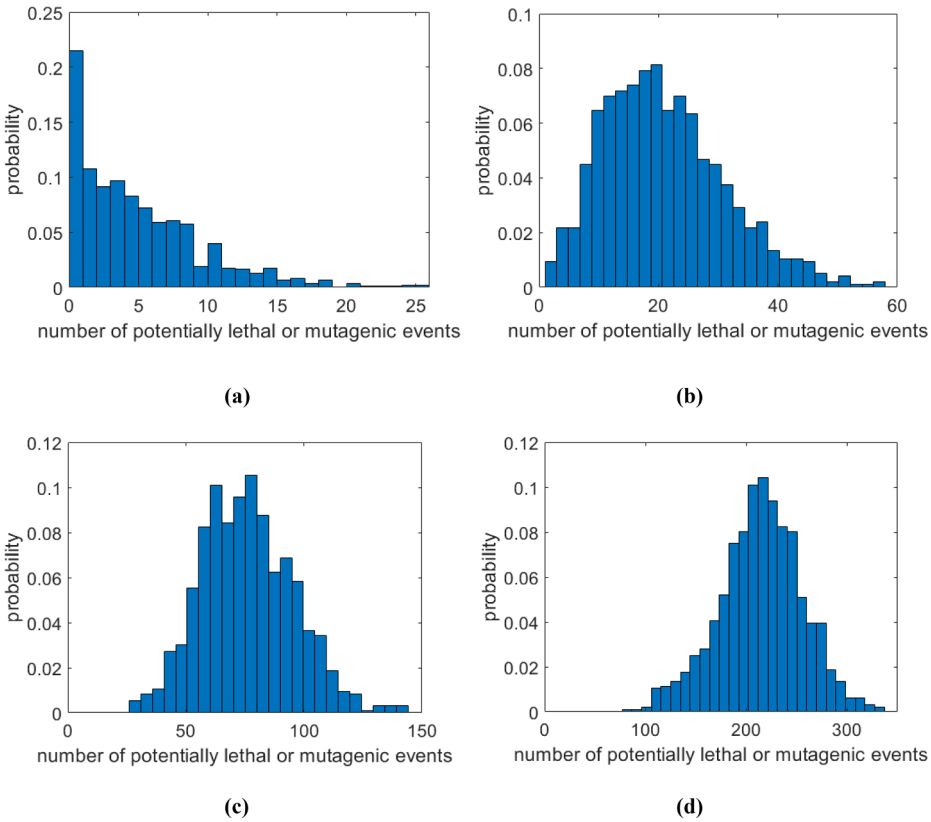


**Fig. 11.** Histograms of the number of PLMEs for 1.0-MeV protons, at different doses. (a) 0.5 Gy, (b) 1 Gy, (c) 2 Gy, and (d) 4 Gy.

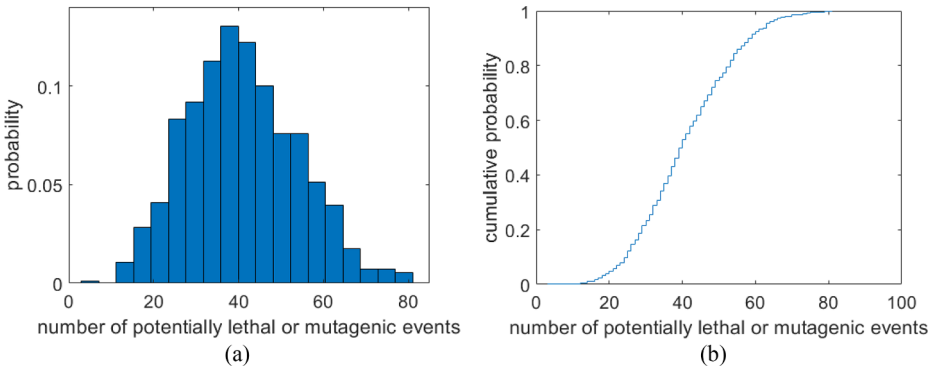


**Fig. 12.** (a) The histogram of the number of PLMEs per cell for 4 Gy of 1-MeV electron irradiation scheme, and (b) the CDF of the number of PLMEs per cell.

very low (~0.04 per cell for 1 mGy). To minimize the statistical uncertainties associated with the DSBs, one may need to process a large number of cells, much greater than the 960 used in this simulation study.

## 5. Conclusions

In the presented work, a new radiobiological model was developed entirely from principles of the Monte Carlo method. The model integrates charged particle track structures from Geant4-DNA and the detailed cell nucleus DNA organizations to quantify DNA and chromatin damage.

Several iterations were exhaustively explored for how to properly position chromatin fibers in the cell nucleus and how to analyze the charged particle track data in order to gain insight into spatially distributed radiation damage patterns. The evaluation demonstrates that the results obtained match well with those obtained from other radiobiological models and experimental results. We have shown that broadly different forms and quantities of radiation can be handled and evaluated efficiently using this new model. Moreover, our model integrates a statistically-correlated element that evaluates variations in potentially lethal or mutagenic events that we believe will offer an effective tool to experimental radiobiologists.

## References

[1] Kellerer A, Rossi H. RBE and the primary mechanism of radiation action. Radiat Res 1971;47:15–34.
[2] Hall E, Giaccia A. Radiobiology for the radiobiologist. 7th ed. Philadelphia: Lippincott Williams & Wilkins; 2012.
[3] Watson J, Crick F. Molecular structure of nucleic acids: a structure for deoxyribose nucleic acid. Nature 1953;171:737–8.
[4] Goodhead D. Inactivation and mutation of cultured mammalian cells by aluminum characteristic ultrasoft x-rays. III. Implications for theory of dual radiation action. Int J Radiat Biol 1977;32(1):43–70.
[5] Goodhead D. An assessment of the role of microdosimetry in radiobiology. Radiat Res 1982;91:45–76.
[6] Bedford J, Mitchell J. Dose-rate effects in synchronous mammalian cells in culture. Radiat Res 1973;54(2):316–27.
[7] Barendsen G, Walter M, Fowler J, Bewley D. Dose–survival curves of human cells in tissue culture irradiated with alpha-, beta-, 20-kV X- and 200-kV X-radiation. Nature 1962;193:1153–5.
[8] Hall E, Novak J, et al. RBE as a function of neutron energy: I. Experimental observations. Radiat Res 1975;64:245–55.
[9] Weyrather W, Ritter S, Scholz M, Kraft G. RBE for carbon track-segment irradiation in cell lines of differing repair capacity. Int J Radiat Biol 1999;75(11):1357–64.
[10] Ando K, Kase Y. Biological characteristics of carbon-ion therapy. Int J Radiat Biol 2009;85(9):715–28.
[11] Luger K, Richmond T. DNA binding within the nucleosome core. Curr Opin Struct Biol 1998;8:33–40.
[12] Hofer K, Lin X, Schneiderman M. Paradoxical effects of iodine-125 decays in parent and daughter DNA: a new target model for radiation damage. Radiat Res 2000;153:428–35.
[13] Olins D, Olins A. Chromatin history: our view from the bridge. Nat Rev Mol Cell Biol 2003;4:809–14.
[14] Cremer T, Cremer C. Chromosome territories, nuclear architecture and gene regulation in mammalian cells. Nature 2001;2:292–301.
[15] Lukasova E, Kozubek S, Kozubek M, Falk M, Amrichova J. The 3D structure of human chromosomes in cell nuclei. Chromosome Res 2002;10:535–48.
[16] Branco M, Pombo A. Chromosome organization: new facts, new models. Trends Cell Biol 2007;17(3):127–34.
[17] Albiez H, Cremer M, et al. Chromatin domains and the interchromatin compartment form structurally defined and functionally interacting nuclear networks. Chromosome Res 2006;14:707–33.
[18] Lanctôt C, Cheutin T, Cremer M, Cavalli G, Cremer T. Dynamic genome architecture in the nuclear space: regulation of gene expression in three dimensions. Nature 2007;8:104–15.
[19] Raju MR, et al. Radiobiology of ultrasoft x rays: I. cultured hamster cells (V79). Radiat Res 1987;110:396–412.
[20] Hill M, et al. Biological effectiveness of isolated short electron tracks: V79–4 cell inactivation following low dose-rate irradiation with Al-K ultrasoft x-rays. Int J Radiat Biol 2002;78:967–79.
[21] Barendsen G. Responses of cultured cells, tumors, and normal tissues to radiations of different linear energy transfer. Curr Topics Radiat Res 1968;4:293–356.
[22] Furusawa Y, et al. Inactivation of aerobic and hypoxic cells from three different cell lines by accelerated $^{3}$He-, $^{12}$C, and $^{20}$Ne-ion beams. Radiat Res 2000;154:485–96.
[23] Folkard M, Prise K, et al. The irradiation of V79 mammalian cells by protons with energies below 2 MeV. Int J Radiat Biol 1989;56(3):221–37.
[24] Blue T, Woollard J, Gupta N, Greskovich J. An expression for the RBE of neutrons as a function of neutron energy. Phys Med Biol 1995;40(5):757–67.
[25] Belli M, et al. RBE-LET relationship for cell inactivation and mutation induced by low energy protons in V79 cells: further results at the LNL facility. Int J Radiat Biol 1998;74(4):501–9.
[26] Franken N, Hovingh S, et al. Relative biological effectiveness of high linear energy transfer α-particles for the induction of DNA-double-strand breaks, chromosome aberrations and reproductive cell death in sw-1573 lung tumour cells. Oncol Rep 2012;27:769–74.
[27] Fowler J. Development of radiobiology for oncology – a personal view. Phys Med Biol 2006;51:R263–86.
[28] Wang C, Zhang X. A nanodosimetry-based linear-quadratic model of cell survival for mixed-LET radiations. Phys Med Biol 2006;51:6087–98.
[29] Wang C, Zhang X, Gifford I, Al-Sheikly M. Experimental validation of the new nanodosimetric cell survival model with mixed neutron and gamma-ray irradiations. Phys Med Biol 2007;52:N367–74.
[30] Scholz M, Elsasser T. Biophysical models in ion beam radiotherapy. Adv Space Res 2007;40:1381–91.
[31] Friedland W, Jacob P, Bernhardt P, Paretzke H, Dingfelder M. Simulation of DNA after proton irradiation. Radiat Res 2003;159:401–10.
[32] Radulescu I, Elmroth K, Stenerlow B. Chromatin organization contributes to non-randomly distributed double-strand breaks after exposure to high-LET radiation. Radiat Res 2004;161:1–8.
[33] Boei J, Fomina J, Darroudi F, Nagelkerke N, Mullenders L. Interphase chromosome positioning affects the spectrum of radiation-induced chromosomal aberrations. Radiat Res 2006;166:319–26.
[34] Kreth G, Pazhanisamy S, Hausmann M, Cremer C. Cell type-specific quantitative predictions of radiation-induced chromosome aberrations: a computer model approach. Radiat Res 2007;167:515–25.
[35] Plante I, Ponomarev A, Cucinotta F. Calculation of the energy deposition in nanovolumes by protons and HZE particles: geometric patterns of initial distributions of DNA repair foci. Phys Med Biol 2013;58:6393–405.
[36] Alloni D, et al. A Monte Carlo study of the radiation quality dependence of DNA fragmentation spectra. Radiat Res 2010;173:263–71.
[37] Wang C. The progress of radiobiological models in modern radiotherapy with emphasis on the uncertainty issue. Mutation Res 2010;704:175–81.
[38] Naqa I, Pater P, Seuntjens J. Monte Carlo role in radiobiological modelling of radiotherapy outcomes. Phys Med Biol 2012;57:R75–97.
[39] Incerti S, et al. The geant4-dna project. Int J Model Simul Sci Comput 2010;01:157–78.
[40] Bernal M, et al. Track structure modeling in liquid water: a review of the Geant4-DNA very low energy extension of the Geant4 Monte Carlo simulation toolkit. Physica Med 2015;31(8):861–74.
[41] Incerti S, et al. Geant4-DNA example applications for track structure simulations in

liquid water: a report from the Geant4-DNA Project. Med Phys 2018;45(8):e722–39.
[42] Incerti S, et al. Comparison of GEANT4 very low energy cross section models with experimental data in water. Med Phys 2010;37(9):4692–708.
[43] Friedland W, Dingfelder M, Kundrat P, Jacob P. Track structures, DNA targets and radiation effects in the biophysical Monte Carlo simulation code PARTRAC. Mutat Res 2011;711:28–40.
[44] Bernal M, Liendo J. An investigation on the capabilities of the PENELOPE MC code in nanodosimetry. Med Phys 2009;36(2):620–5.
[45] Nikjoo H, Girard P. A model of the cell nucleus for DNA damage calculations. Int J Radiat Biol 2012;88(1–2):87–97.
[46] Semenenko V, Stewart R. Fast Monte Carlo simulation of DNA damage formed by electrons and light ions. Phys Med Biol 2006;51:1693–706.
[47] Friedrich T, Durante M, Scholz M. Modeling cell survival after photon irradiation based on double-strand break clustering in megabase pair chromatin loops. Radiat Res 2012;178:385–94.
[48] Friedrich T, Durante M, Scholz M. Modeling cell survival after irradiation with ultrasoft X Rays using the Giant Loop Binary Lesion Model. Radiat Res 2014;181:485–94.
[49] Lee B. A Monte Carlo investigation of radiation damage to chromatin fibers and production of DNA double strand breaks using Geant4-DNA code [masters thesis] Atlanta (GA): Georgia Institute of Technology; 2014.
[50] Date H, Sutherland K, Hasegawa H, Shimozuma M. Ionization and excitation collision processes of electrons in liquid water. Nucl Instrum Meth phys Res B 2007;265:515–20.
[51] Ziegler J, Biersack J, Ziegler M. SRIM – The stopping and range of ions in matter. Ion Implantation Press; 2008.
[52] Meylan S, et al. Simulation of early DNA damage after the irradiation of a fibroblast cell nucleus using Geant4-DNA. Sci Rep 2017(7).
[53] Friedland W, et al. Comprehensive track-structure based evaluation of DNA damage by light ions from radiotherapy-relevant energies down to stopping. Sci Rep 2017;7..
[54] Morton N. Parameters of Human Genome. Proc Natl Acad Sci 1991;88:7474–6.
[55] Friedland W, Kundrat P. Track structure based modelling of chromosome aberrations after photon and alpha-particle irradiation. Mut Res 2013;756:213–23.
[56] Carter L, Cashwell E. Particle-transport simulation with the Monte Carlo method. Los Alamos (NM). Los Alamos Scientific Laboratory; 1975. Technical Report TID-26607.
[57] Peplow D. Direction cosines and polarization vectors for monte carlo photon scattering. Nucl Sci Eng 1999;131:132–6.
[58] Ester M, Kriegel H, Sander J, Xu X. A density-based algorithm for discovering clusters in large spatial databases with noise. AAAI Press; 1996. p. 226–31.
[59] Francis Z, Incerti S, et al. Monte Carlo simulation of energy-deposit clustering for ions of the same LET in liquid water. Phys Med Biol 2012;57:209–24.
[60] Lee B. A Monte Carlo-based simulation study for assessing radiation-induced DNA damage and cell survival [dissertation]. Atlanta (GA): Georgia Institute of Technology; 2017.
[61] Folkard M, et al. Measurement of DNA damage by electrons with energies between 25 and 4000 eV. Int J Radiat Biol 1993;64(6):651–8.
[62] Sachs R, Chen A, Brenner D. Review: proximity in the production of chromosome aberrations by ionizing radiation. Int J Radiat Biol 1997;71(1):1–19.
[63] Chen A, Lucas J, Hill F, Brenner D, Sachs R. Proximity effects for chromosome aberrations measured by FISH. Int J Radiat Biol 1996;69:411–20.
[64] Savage J. Insight into sites. Mutation Res 1996;366:81–95.
[65] Edwards A, Moiseenko V, Nikjoo H. On the mechanism of the formation of chromosomal aberrations by ionizing radiation. Radiat Environ Biophys 1996;35:25–30.
[66] Sachs R, Levy D, Chen A, Simpson P, Cornforth M, Ingerman E, et al. Random breakage and reunion chromosome aberration formation model; an interaction-distance version based on chromatin geometry. Int J Radiat Biol 2000;76(12):1579–88.
[67] Holley W, Mian I, Park S, Rydberg B, Chatterjee A. A model for interphase chromosomes and evaluation of radiation-induced aberrations. Radiat Res 2002;158:568–80.
[68] Pater P, Seuntjens J, El Naqa I, Bernal M. On the consistency of Monte Carlo track structure DNA damage simulations. Med Phys 2014;41(12).
[69] De Lara C, Hill M, Jenner T, Papworth D, O'Neill P. Dependence of the yield of DNA double-strand breaks in Chinese hamster V79–4 cells on the photon energy of ultrasoft X Rays. Radiat Res 2001;155:440–8.
[70] Frankenberg D, et al. Induction of DNA double-strand breaks by $^{1}H$ and $^{4}He$ ions in primary human skin fibroblasts in the LET range of 8 to 124 keV/μm. Radiat Res 1999;151(5):540–9.
[71] Belli M, et al. DNA fragmentation in mammalian cells exposed to various light ions. Adv Space Res 2001;27(2):393–9.
[72] Belli M, et al. DNA DSB induction and rejoining in V79 cells irradiated with light ions: a constant field gel electrophoresis study. Int J Radiat Biol 2000;76(8):1095–104.
[73] Heilmann J, Taucher-Scholz G, Kraft G. Induction of DNA double-strand breaks in CHO-K1 cells by carbon ions. Int J Radiat Biol 1995;68:153–62.
[74] Lampe N, et al. Mechanistic DNA damage simulations in Geant4-DNA Part 2: electron and proton damage in a bacterial cell. Physica Med 2018;48:146–55.
[75] Stewart R, et al. A comparison of mechanism-inspired models for particle relative biological effectiveness (RBE). Med Phys 2018;45(11):e925–52.
[76] Kamp F, et al. Fast biological modeling for voxel-based heavy ion treatment planning using the mechanistic repair-misrepair-fixation model and nuclear fragment spectra. Int J Radiat Oncol Biol Phys 2015;93(3):557–68.
[77] Hawkins RB. A microdosimetric-kinetic model for the effect of non- Poisson distribution of lethal lesions on the variation of RBE with LET. Radiat Res 2003;160:61–9.